Local Time- and Space Scales of Organized Tropical Deep Convection

LUCREZIA RICCIARDULLI* AND PRASHANT D. SARDESHMUKH

NOAA–CIRES Climate Diagnostics Center, University of Colorado at Boulder, Boulder, Colorado

(Manuscript received 14 February 2001, in final form 9 April 2002)

ABSTRACT

The time- and space scales of tropical deep convection are estimated via analysis of 3-hourly Global Cloud Imagery (GCI) data for 3 yr at 35–70-km resolution. The emphasis is on estimating *local* time- and space scales rather than traditional zonal wavenumber–frequency spectra. This is accomplished through estimation of local spatial lag autocorrelations, the conditional probability of convection at neighboring points, and the expected duration of convective events. The spatial autocorrelation scale is found to be approximately 130 km, and the mean duration of convective events approximately 5.5 h, in the convectively active areas of the Tropics. There is a tendency for the spatial autocorrelation scales to be shorter over the continents than oceans (95–155 versus 110–170 km). The expected duration of convective events likewise tends to be shorter (4–6 versus 5–7 h). In the far western Pacific, these differences are sharp enough to legitimize the notion of the Indonesian archipelago as an extended maritime continent with a distinctive shape. Consistent with many other studies, the diurnal variation of the convection is also found to be strikingly different over the continents and oceans. The diurnal amplitude over land is comparable to the long-term mean, raising the possibility of significant aliasing across timescales. The simple analysis of this paper should be useful in evaluating and perhaps even improving the representation of convective processes in general circulation models.

1. Introduction

Many aspects of the mean tropical climate and its variability cannot be understood without accounting for the release of latent heat in deep convective clouds. The effects of convection also extend well beyond the Tropics into middle and high latitudes through Rossby wave propagation (e.g., Hoskins and Karoly 1981; Sardeshmukh and Hoskins 1988; Ting and Sardeshmukh 1993). Indeed extratropical predictability beyond that of synoptic weather is viable primarily because of predictable tropical influences (e.g., Opsteegh and Van den Dool 1980; Horel and Wallace 1981; Palmer and Anderson 1994; Peng et al. 2000; Sardeshmukh et al. 2000; Winkler et al. 2001). Tropical convective clouds also affect the atmospheric radiation balance, making their correct representation critical in climate models used in global warming research. Additionally, convectively forced vertically propagating equatorial waves affect the dynamics of the stratospheric semiannual and quasi-biennial zonal wind oscillations, and hence the behavior of long-lived stratospheric chemical species (e.g., Tung and Yang 1994; Ray et al. 1994).

Despite many efforts, the representation of tropical convection remains a challenge for general circulation modelers. The processes associated with convection and cloud formation generally occur on scales not resolved by general circulation models (GCMs). Convection must therefore be parameterized, that is, represented in terms of resolved model variables. This always involves making closure assumptions (Arakawa 1993). The parameterization schemes currently employed in GCMs range from simple convective adjustment (Manabe et al. 1965; Betts and Miller 1986; Kuo 1974) to complicated mass flux schemes (Arakawa and Schubert 1974; Tiedtke 1989; Zhang and McFarlane 1995). Many studies have highlighted the sensitivity of the simulated weather and climate to the particular choice of scheme (e.g., Slingo et al. 1994; Hess et al. 1993; Slingo et al. 1996; Maloney and Hartmann 2001; Ricciardulli and Garcia 2000). Some schemes are more sophisticated than others, but at present none can be claimed to represent realistically the temporal and spatial variability of the observed convection. In their intercomparison study of 31 atmospheric GCMs, Gates et al. (1999) identified the parameterization of convection and precipitation, and of clouds and their radiative interactions, as ''continuing outstanding problems'' in atmospheric modeling.

Part of the difficulty lies with validation. Most pa-

* Current affiliation: Remote Sensing Systems, Santa Rosa, California.

Corresponding author address:: Dr. Prashant D. Sardeshmukh, NOAA–CIRES Climate Diagnostic Center, David Skaggs Research Center, 325 Broadway, Boulder, CO 80305.
E-mail: pds@cdc.noaa.gov

rameterization schemes contain parameters whose proper values are indeterminate either because they are not directly comparable with observational data or because of a lack of data. An alternative is to tune the parameters to match the output of the scheme to observations, which is often done in single-column tests using data from field experiments. Such tests have their own limitations. For example, it is not clear to what extent their results are applicable in conditions other than those during the field experiments. More seriously, such tests ignore the interaction between the circulation and convection dynamics by artificially decoupling the adiabatic and diabatic tendencies at a grid point. To the extent that the coupling is important in determining the time- and space scales of convective variability, the tuning occurs with a blind eye toward its effect on those scales.

Given that the design of a convection scheme has direct implications for the time- and space scales of a model's simulated convective variability, it should ideally be done with those scales in mind. A first step in this direction is to determine the time- and space scales of the observed variability. These are often discussed in terms of zonal wavenumber–frequency spectra. The spectral description was originally motivated by a need to verify equatorial wave theory and to investigate tropical phenomena in the context of that theory. It continues to be useful in the diagnosis of equatorial stratospheric phenomena (e.g., Ricciardulli and Garcia 2000). For diagnosing tropical tropospheric motions and especially model errors, however, its interpretation is less direct. For example, distinctions that may exist between continental and oceanic convection along a latitude circle are lost. A wavenumber–frequency description is nonlocal, and while mathematically always valid, is easiest to interpret when the statistics of the variability are homogeneous in space and time. Such would indeed be the case for a randomly excited model atmosphere with zonally symmetric boundary conditions. However, it is not true of the observed Tropics with its zonal land–sea contrasts and three distinct areas of organized convective variability. Still, some insight into the local features of organized convection can be achieved through spectral analysis in limited regions (e.g., Salby et al. 1991). In such an analysis, fluctuations of convective activity that are coherent over the domain are highlighted in the spectrum of the domain average. However, even this approach does not yield simple quantitative measures of the dominant time- and space scales of organized convection over the domain.

A spectral description is directly useful when the variability is strongly wavelike, that is, when the spectrum displays sharp peaks. The spectra of tropical convection, however, display a broadband character in both the frequency and wavenumber domains (e.g., Bergman and Salby 1994). Indeed, apart from the annual and diurnal peaks and their harmonics, spectral peaks do not account for a major portion of the total power of tropical convective variability. Recent work by Wheeler and Kiladis (1999) has suggested the existence of peaks along the dispersion curves of equatorial waves in the zonal wavenumber-frequency domain. These peaks too are rather diffuse, and as discussed by Wheeler and Kiladis, are dwarfed by the red noise background in both the wavenumber and frequency directions.

Our principal aim here is not to criticize the traditional spectral representation of tropical variability, but rather to shift the focus to the red background. In our view, it should not be dismissed as irrelevant noise, because to the extent that it dominates the spectrum, the important time- and space scales of tropical convective variability are the spatial and temporal correlation scales of that noise. If a substantial part of the variability is noise, then it is surely just as relevant for a GCM to represent its statistical structure as that of the more wavelike modes of the variability.

By statistical structure we mean here the geographical distribution of the local spatial and temporal lag-autocorrelations. This paper describes one attempt to establish these aspects of tropical deep convection. Cloud observations from satellites represent the optimal data source for this purpose, as relatively long time series with high spatial and temporal resolution and uniform tropical coverage are desirable. Specifically, our analysis is conducted using three-hourly fields of global cloud imagery (GCI) data (see Salby et al. 1991) for three complete years at $\sim$70 km resolution in longitude and $\sim$35 km in latitude. The local time- and space scales of convection as revealed by these proxy cloud data are estimated through local spatial lag-autocorrelations, the conditional probability of convection at neighboring grid points, and the expected duration of convective events. These basic quantities are documented on scales of direct relevance to GCMs. In particular, the tropical maps presented here highlight the distinction between continental and oceanic convection, and allow *regional* comparisons with model output. They represent a simple diagnostic tool that, in conjunction with spectral analysis, should be useful in evaluating and perhaps even improving the representation of convective processes in GCMs. Our approach also complements that of Boer and Ramanathan (1997) and Laing and Fritsch (1997), who attempt to establish the scales of organized tropical convection through rather different methods.

The GCI data and the conversion of the satellite radiance measurements to an index of deep convective activity (DCA) are described in section 2. The statistics of DCA at the full resolution of the data are presented in section 3. Some statistics of DCA averaged over 2.8° $\times$ 2.8° grid boxes typical of many current climate models are presented in section 4. Examples of similar statistics from two different GCMs are provided in section 5, and concluding remarks are made in section 6.

2. Cloud observations: The GCI dataset

Our basic dataset consists of satellite cloud observations from the International Satellite Cloud Clima-

TABLE 1 Months during 1983–92 for which the GCI data were available. Only those months marked by an uppercase X were used in this study.

	1983	84	85	86	87	88	91	92
Jan		X		X				X
Feb		X		X				X
Mar		X	x	X				X
Apr		X	x	X				X
May		X	x	X				X
Jun		X	x	X	x			X
Jul	X		X	x	X			x
Aug	X		X	x	X			x
Sep	X		X	x	X	x		
Oct	X		X	x	X	x		
Nov	X		X	x	X	x		
Dec	X		X	x	X		x	

tology Project (ISCCP; Schiffer and Rossow 1983). It includes intercalibrated measurements from four geostationary and two polar-orbiting satellites. The ISCCP observations of cloud infrared radiances were processed by Salby and coworkers (Tanaka et al. 1991; Salby et al. 1991; Woodberry et al. 1991) to create a synoptic dataset of global cloud fields, the global cloud imagery GCI dataset. This GCI dataset has been used here without further spatial or temporal filtering.

Salby and coworkers used the infrared (IR) radiances from the 11-μm channel of each satellite in the ISCCP ''B3'' archive to create the GCI dataset. A correction due to satellite viewing geometry was made (Tanaka et al. 1991) to account for systematic errors in the IR radiances at low zenith angles (see also Joyce and Arkin 1997). As described in section 2 of Tanaka et al, cloud image pixels were selectively sampled and collected in regular $0.35° \times 0.7°$ latitude–longitude boxes at 3-hourly intervals. Because the values on the 512×512 global grid were obtained from samples and do not strictly represent $0.35° \times 0.7°$ and 3-h averages, the effective resolution of the GCI dataset is somewhat higher than implied by those averages.

Due to discontinuities in the operation of different satellites, only data for the 53 months listed in Table 1 in 1983–92 were available. To avoid disproportionate emphasis on certain calendar months than others, our analysis was further restricted to 36 of those 53 months, comprising three complete years with three samples of each calendar month. All observational results presented here are based on this 36-month dataset. The entire analysis was also repeated with the full 53-month dataset, and gave nearly identical results (not shown).

An equivalent blackbody brightness temperature (TBR) of the clouds can be derived from the IR radiances at 11 μm. The TBR reflects fluctuations of cloud-top height, and serves as a proxy of the latent heat released in tropical deep convection. To discriminate between radiances from deep convective and shallow clouds, only clouds colder than 240 K (corresponding to approximately the 300-mb level) were considered. The deep convective activity index was defined as:

$$\mathrm{DCA} = \begin{cases} 240 - \mathrm{TBR} & \text{if TBR} < 240 \text{ K} \\ 0 & \text{otherwise.} \end{cases} \quad (1)$$

This is similar to the definition adopted by Hendon and Woodberry (1993) except for a slightly different choice of the threshold. Areas of cloud cover colder than 240 K correspond well with those of observed precipitation (Richards and Arkin 1981). As described in Ricciardulli and Garcia (2000), this DCA index can also be converted to a more direct estimate of the column-averaged deep convective heating rate (DCH), expressed in units of K day^{-1} as DCH = 0.87 DCA. Since this generally refers to latent heat release, we also associate positive DCA (and DCH) with ''wet'' events. We should stress, however, that DCA is used in this study mainly to indicate the *presence* of deep convection and its spatial and temporal scales. Its quantitative link with precipitation, while useful, is not our primary focus.

As discussed by Hendon and Woodberry (1993), the choice of a constant brightness temperature threshold [240 K in (1)] has some limitations, as it can cause thin and high cold cirrus clouds to be erroneously grouped with deep convective clouds. One way around this is to consider also the visible (VS) band and discriminate convective clouds by imposing another threshold on the VS reflectance R (Fu et al. 1990). In this combined VS–IR method, deep convective clouds are associated with TBR < 240 K and $0.6 < R < 0.8$. This method was not applied to our dataset since we did not have the VS observations available. Still, our choice of the 240-K threshold is consistent with scatterplots of VS reflectances versus IR radiances (Fu et al. 1990, their Fig. 2) showing that brightness temperatures lower than 240 K seldom correspond to the low VS reflectances typical of cirrus clouds. Cirrus clouds have also lower variability in space and time than deep convective clouds, and so we do not expect them to have a strong influence on our statistical analysis. As a further check, we repeated some of our calculations with thresholds of 230 and 220 K, and obtained generally similar results to those shown here.

3. Analysis of tropical convection

Many studies of tropical variability focus on the evolution of daily averaged precipitation or outgoing longwave radiation (OLR) and their association with the large-scale circulation on synoptic and longer timescales. However, some recent studies (e.g., Slingo et al. 1994; Ricciardulli and Garcia 2000) suggest that some of the difficulties of GCMs in simulating tropical dynamics may be related to the misrepresentation of convection on shorter time- and space scales. Our aim here is therefore to summarize the general characteristics of observed convection on these shorter scales, with a view of providing verification targets for GCM simulations.

The results presented here are based on the statistics of DCA in the ''convectively active'' months in our 36-

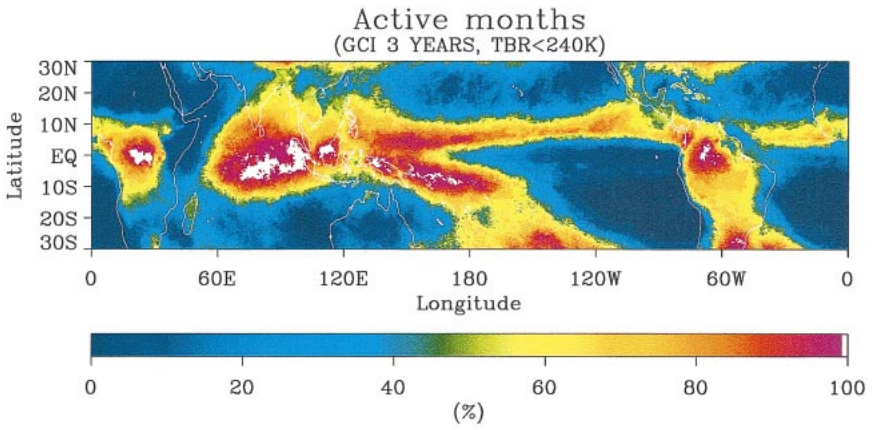

FIG. 1. Percentage of convectively active months in the 36-month GCI dataset.

month dataset, defined at each grid point as months in which DCA is positive at least 5% of the time. Given that the data consists of 3-hourly samples with 8 values per day, this means that a month is declared convectively active if at least 12 of the 240 3-hourly values in the month have positive DCA. Our decision to stratify the data into active and inactive months, as opposed to say summer and winter months, was motivated by a concern that some statistical measures of convection could be greatly distorted by including extended dry periods in the analysis. It was also affected by a desire to increase sample sizes to generate more reliable statistics. Also, physically based parameterizations of convection have quasi-universal validity: one does not have different parameterizations for winter and summer convection. We therefore examined the characteristics of convection at each tropical grid point without regard to season. This means that the maps presented here are not interpretable in any simultaneous (or ''synoptic'') sense, since they summarize the characteristics of deep convection at different times of year at different locations, especially in the monsoon regions of India and Central America. Another consequence of our restriction to active months is that we cannot say anything about the occasional convective activity that occurs in the climatologically arid regions of the Tropics and subtropics.

Figure 1 shows the geographical distribution of the fraction of convectively active months in our 36-month dataset. Apart from setting the context of this study, the figure is also useful in sharply delineating the regions of almost-constant, almost-absent, and seasonal (or perhaps more accurately, monsoonal) convective activity. As such it represents an interesting target for GCMs that is distinct from, say, a map of annual mean rainfall. Note that Fig. 1 is not very sensitive to the choice of the 5% threshold used to define the ''active'' months. A 10% threshold produces a similar map with slightly reduced amplitude (not shown).

a. Timescales

Figure 2 highlights the fact that deep convective activity is highly variable within the active months. Figure 2a shows the probability p of convective precipitation during the active months, estimated as the percentage of the total 3-hourly DCA values for which DCA is positive. The probability tends to be relatively high near the maxima in Fig. 1. Even in these regions, however, it is noteworthy that it ''rains'' only about 20%–25% of the time in the active months.

Figure 2b shows the expected duration of ''wet'' events, defined as DCA > 0. At each grid point, the probability density function $P(t_w)$ of wet-event durations t_w was estimated through a histogram analysis, and the figure shows the expected mean value $\langle t_w \rangle = \Sigma\, t_w\, P(t_w)$. Note that the lowest significant limit of $\langle t_w \rangle$ is 1.5 h due to the 3-hourly resolution of the GCI data. If all the ''rain'' occurs within a 3-h segment, we assume the probability of its duration to be uniformly distributed between 0 and 3 h, and estimate $\langle t_w \rangle$ as 1.5 h. A distinction in the behavior of convection is evident over the continents and oceans. Precipitation events tend to be shorter over the continents (4–6 h), and somewhat more persistent over the oceans (5–7 h). An exception occurs over India, where the timescale is similar to that over the Indian Ocean. It should be emphasized, however, that our results are least reliable in a swath around 60°–70°E, where geostationary satellite observations were unavailable and only polar-orbiting satellites with twice-daily crossings could be used. Sampling and interpolation errors are probably behind the appearance of the suspicious vertical strips and ''crop circle'' patterns in this longitude sector in Fig. 2 and in most of the other maps presented here.

A noteworthy feature of Fig. 2b is the shorter duration of convection over an extended area around the Indonesian islands, New Guinea and Borneo. This contrasts with the longer timescales over the surrounding ocean,

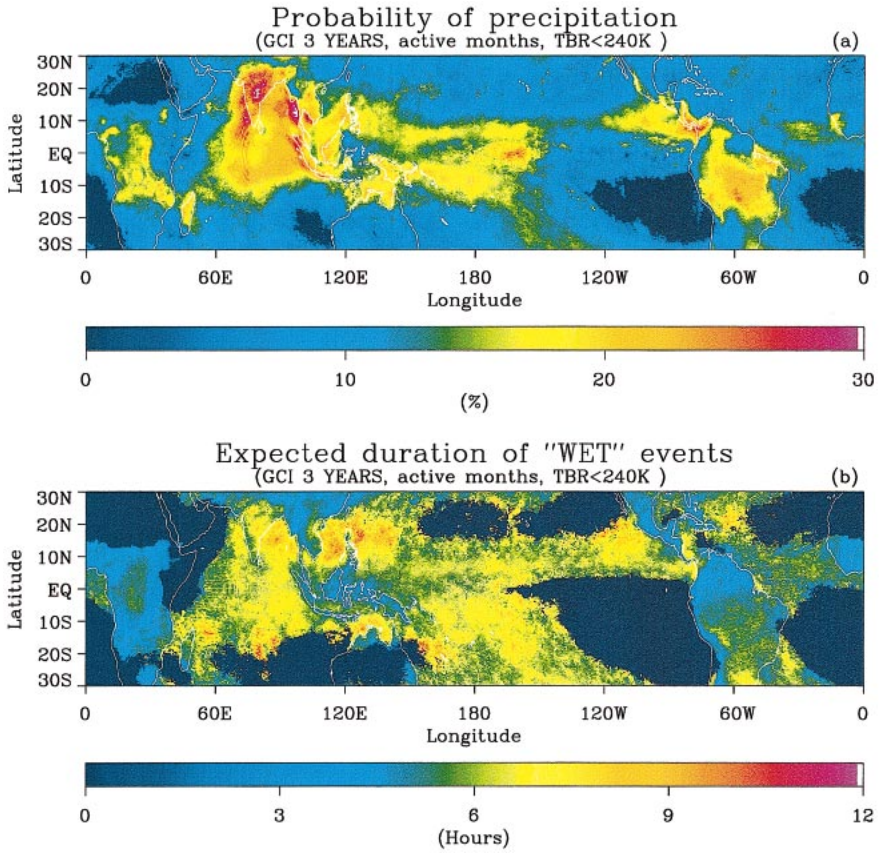

FIG. 2. (a) Probability of precipitation (i.e., positive DCA) and (b) expected duration of wet events during the active months.

and justifies the notion of a west Pacific ''Maritime Continent'' with a distinctive shape.

Figure 3 summarizes the information of Fig. 2b in a histogram format. It shows the distributions of timescales $\langle t_w \rangle$ over the land and ocean areas in Fig. 2b. The mean (± 1 standard deviation) of the continental and oceanic values are 4.9 (± 0.8) and 6.2 (± 0.9) h, respectively. Although the overlap between the distributions is considerable, the general tendency for the timescales to be shorter over the continents than the oceans is clear.

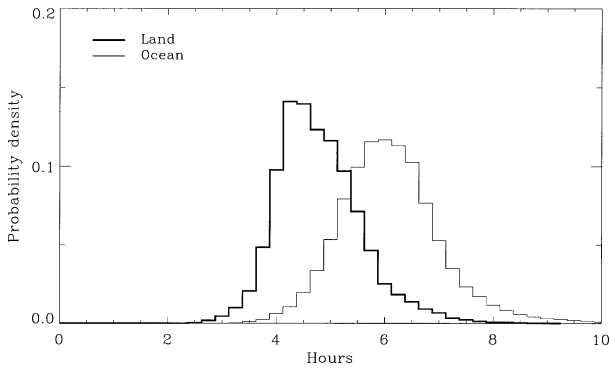

FIG. 3. Histograms of mean duration of wet events over the land and ocean areas in Fig. 2.

The distribution over land is also apparently more skewed than its oceanic counterpart in Fig. 3. It is possible that this is due to our inability to resolve wet events lasting less than 3 h. The question is, would the land distribution in Fig. 3 be ''filled out'' and shifted even farther to the left if we had, say, 1-hourly data? If yes, our current estimates of the land scales would be in error, but the distinction between the land and ocean scales would then become even more dramatic. Actually, the answer to the above question is probably no, because the peak of the land distribution in Fig. 3 is at 4 h, not 3 h. There is also a possibility that the land distribution appears positively skewed because of the inclusion of longer-duration events over regions such as subtropical South America that might be associated more with synoptic variability.

b. Space scales

The local spatial scales of deep convection were estimated using two different approaches, one based on the separation distance at which the DCA values become

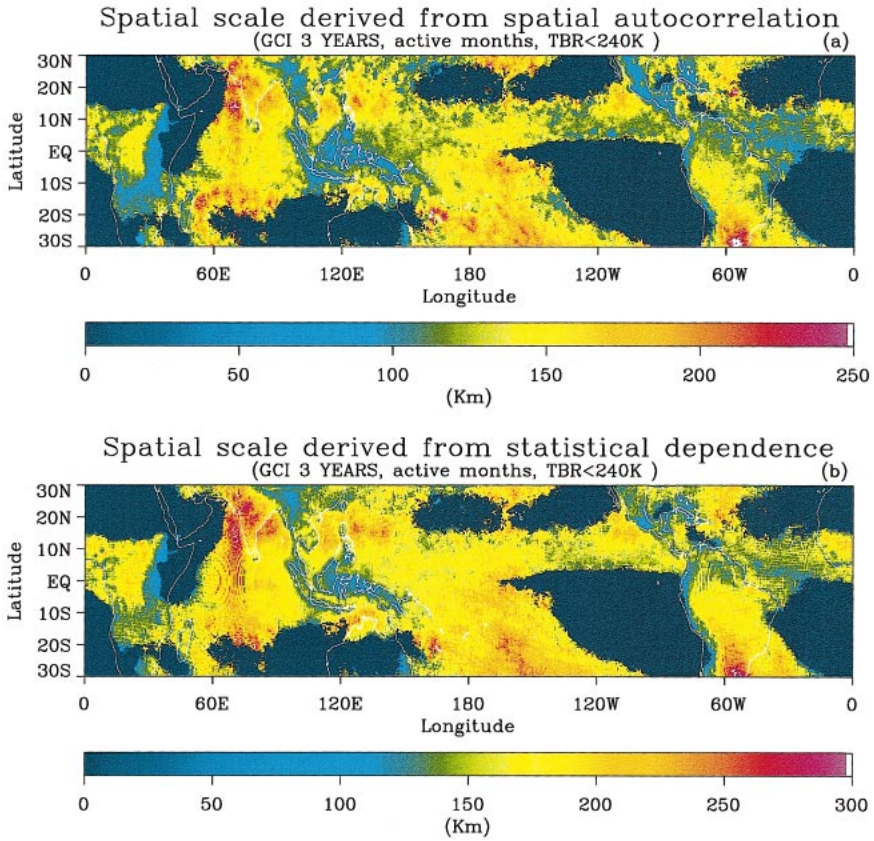

FIG. 4. Spatial scale of deep convection estimated as (a) distance at which the spatial lag autocorrelation of DCA falls to 1/*e*, and (b) the separation distance at which DCA values become statistically independent, in the sense described in the text.

linearly uncorrelated, and the other on the distance at which they become statistically independent.

In the first method, for each grid point on the 0.35° × 0.70° grid, the decay of the spatial autocorrelation of DCA with distance was estimated by averaging the correlations at equidistant surrounding points. (Care was taken to use only values in the common active months in this calculation.) The local spatial scale r_0 of the convection at the grid point was then defined as the distance from the grid point at which the correlation falls to 1/*e*. Figure 4a shows the geographical variation of the values of r_0 thus obtained. Contrasting behavior is again evident over the continents and oceans, although perhaps not as sharply as in Fig. 2b. The values of r_0 over land (including the Maritime Continent) are typically 90–150 km, whereas they are 115–175 km over the oceans. The major exception to this distinction is again over India, where r_0 is similar to that over the Indian Ocean. As before, one might attribute this to the available satellites not being able to see this region very well. Still, there are other exceptions to a claim of shorter scales over land that cannot be glossed over, such as subtropical South America, where r_0 is in fact larger than at any other point in Fig. 4a. Regardless of whether this reflects the subtropical tail of extratropical weather systems (James and Anderson 1984) or an erroneous interpretation of DCA at subtropical latitudes as truly indicative of ''deep convective activity,'' the danger of overgeneralization is clear. An even more notable exception is the tropical Atlantic sector, where r_0 over the ocean is smaller than over the African continent immediately to its east.

In the second method, the spatial scales of convective events were deduced using a probabilistic approach. We first estimated the conditional probability $P_c[w(r) \mid w(0)]$ of wet events at distances r from each grid point, given the occurrence of a wet event at the grid point. (Again, this was done by averaging the conditional probabilities at equidistant points, taking care to consider only the common active months.) At small distances P_c is close to 1. At distances of 250 km and greater, it approaches the marginal (i.e., the unconditional) probability p of precipitation (shown in Fig. 2a) at the remote points, since the probability of precipitation at those points becomes increasingly independent of that at the central point. Given that p in Fig. 2a is nearly constant over the 100–250-km scales of interest here, we approximated p at the remote points as p at the central point. The P_c associated with each central grid point was then modeled as decaying exponentially with distance from

1 to p. In other words, the standardized conditional probability $D(r) = (P_c - p)/(1 - p)$, which may also be interpreted as a measure of the statistical dependence of convection at points separated by distance r, was modeled as decaying exponentially from 1 to 0:

$$D(r) = [P_c - p]/[1 - p] \approx \exp(-r/r_0). \qquad (2)$$

The spatial scale r_0 of the convection was defined as the distance at which $D(r)$ falls to $1/e$. Figure 4b shows the geographical variation of r_0 thus obtained. Because DCA is a positive quantity with highly non-Gaussian statistics, this estimate of the scale of the convection as the distance over which convective events become statistically independent need not be the same as the distance over which they become linearly uncorrelated. Even so, the values in Fig. 4b are similar to those in Fig. 4a, though with a tendency towards higher values. The overall similarity of Figs. 4a and 4b is reassuring. Both suggest a tendency for shorter spatial scales over the continents than the oceans, with the same notable exceptions. The Indonesian region again emerges as an extended Maritime Continent with the same distinctive shape in both maps, which is also similar to the shape in Fig. 2b.

Figure 5 summarizes the information of Fig. 4 in a histogram format similar to that of Fig. 3. It shows the distributions of spatial scales over the continents and oceans, obtained by the linear-autocorrelation method (Fig. 5a) and the statistical-dependence method (Fig. 5b). In Fig. 5a, the means (± 1 standard deviation) of the continental and oceanic distributions are 124 (± 30) and 139 (± 28) km, respectively. In Fig. 5b, these same quantities are 158 (± 36) and 176 (± 30) km, respectively. Although the continental and oceanic distributions are not as far apart in Fig. 5 as in Fig. 3, their separation is statistically highly significant.

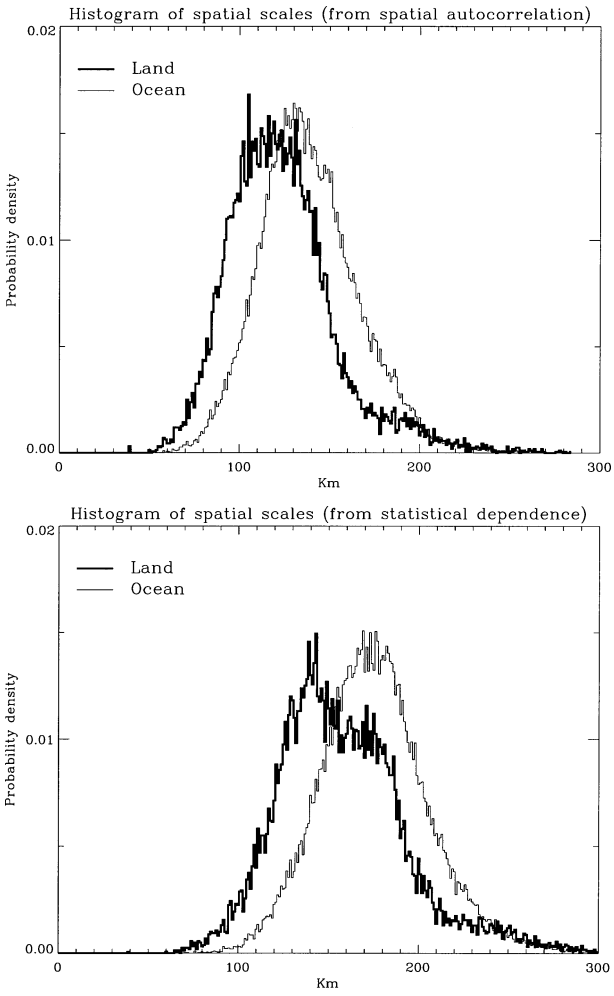

FIG. 5. Histograms of spatial scales of deep convection over the land and ocean areas in Figs. 4a,b.

c. Diurnal cycle

Considering again only the active months, the DCA data were averaged to form a composite day of eight 3-hourly values at each grid point. No spectral analysis was performed. The amplitude of the diurnal cycle was defined as the standard deviation about the mean DCA of the composite day.

The ratio of the amplitude of the diurnal cycle to the composite daily mean is shown in Fig. 6a. Once again a distinction emerges between convection over the continents and oceans. The continents, including the Maritime Continent, show large diurnal variations. The variations are much smaller over the oceans. Notable exceptions to this distinction are again subtropical South America at 30°S, and high-elevation sites in the Andes and Himalayas.

The GCI data are stored in eight nonoverlapping 3-h segments in coordinated universal time (UTC), which effectively creates eight artificial ''time zones.'' To calculate the diurnal maximum of convective activity, data of the composite day was converted to local standard time (LST) at each grid point. The time of the diurnal maximum at the grid point was then defined and determined as the time of peak convective activity in the composite day, rather than as the peak time of the diurnal harmonic fitted to the composite day. Figure 6b shows the local time of the diurnal maximum thus calculated. Given our definition of the diurnal maximum and the discrete 3-hourly GCI data, the sampling uncertainty of these estimates is 3 h. The discontinuities across longitude lines at 45° intervals in the plot are a result of the eight artificial time zones. They arise from neighboring points on opposite sides of these lines with even small differences ε in their estimated times of diurnal maximum being assigned different 3-h slots. The average discontinuity across these lines should therefore be ≤ 3 h, and indeed it is (2.5 h). At some points, however, discontinuities of as large as 6 h are evident. The uncertainty at these points is actually $3 + \varepsilon$ hours as elsewhere in the domain, but is amplified to 6 h at the edges of the time zones for the reason given above.

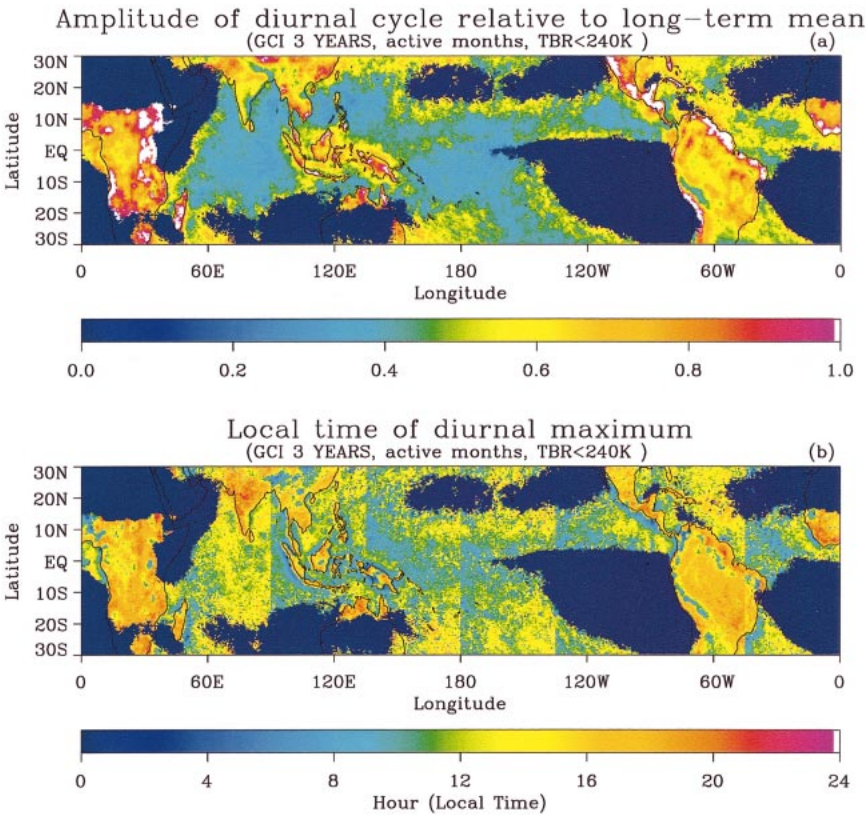

FIG. 6. (a) Amplitude of diurnal cycle of DCA relative to that of long-term mean DCA, and (b) local standard time (LST) of the diurnal maximum of DCA during the convectively active months.

Note that the discontinuities are largest over the oceans, where the small diurnal amplitude makes the estimation of diurnal phase relatively more vulnerable to sampling error.

Figure 6b again shows distinctive convective behavior over land and ocean, particularly in coastal regions. Over land, the maximum occurs in late afternoon around 1600–2000 LST, with some regions such as India and the northern edge of South America exhibiting significantly later maxima. Over the oceans, the maxima occur much earlier, around 0800–1400 LST. The high resolution of GCI data allows other interesting features to emerge from the analysis, such as a dependence of the diurnal phase on orography. Morning maxima (0800–1200 LST) are observed over the mountainous regions of Africa and South America. The maxima occur even earlier (0600–0800 LST) on the west coast of Africa, Central and South America, and around the islands of the Maritime Continent. These early morning maxima are probably associated with land–sea breeze circulations. Another interesting detail is the early morning maximum over Lake Victoria (35°E, equator), resulting from the thermal contrast between the lake and the surrounding mountains (Desbois et al. 1988).

The values in Fig. 6b are slightly sensitive to the temperature threshold of 240 K used to define DCA in (1). Smaller thresholds of 230 and 220 K result in earlier diurnal maxima over the oceans, but not over land (not shown). The analysis of the diurnal cycle was also repeated by considering the complete time series. The results were generally similar to those presented here for the active months alone, but rather noisy, particularly over the oceans. The maps also did not show the longitudinal discontinuities as clearly as Fig. 6b.

We are primarily concerned here with the general features of tropical deep convection and not with a detailed analysis of its diurnal variation. The recent literature contains much more detailed studies of diurnal variations, although they tend to be regional in scope and emphasize specific seasons (Duvel and Kandel 1988; Duvel 1989; Hendon and Woodberry 1993; Bergman and Salby 1996; Chen and Houze 1997). After this paper was submitted for publication, a comprehensive analysis of tropical diurnal variations by Yang and Slingo (2001) using a different quality-controlled version of the GCI dataset appeared in the literature. The reader is referred to their paper, and also to Imaoka and Spencer (2000), who used Special Sensor Microwave Imager (SSM/I) and Tropical Rainfall Measuring Mission (TRMM) data, for detailed discussions of this aspect of tropical convective variability. The main point we wish to emphasize here is that the time-mean convection over

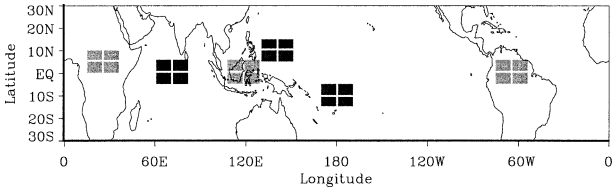

FIG. 7. Three land and three ocean areas used to construct summary statistics in Figs. 8 and 9.

the tropical continents reflects the very strong diurnal cycle there, that is, it is essentially a rectified version of the diurnal variation. This makes it important to ensure the correct representation of the diurnal cycle in GCMs, as it can directly affect the time-mean climatology of the simulated convective heating. Another aspect worth emphasizing is the sharp distinction between the times of diurnal maxima over continental, coastal, and mountainous regions. These emerge more clearly in our analysis, restricted to convectively active months, than in some previous global studies such as those of Hendon and Woodberry (1993) and Yang and Slingo (2001), who obtained noisier results.

d. Summary

Figures 2–6 emphasize the highly irregular character of tropical deep convective activity in both space and time. Our simple statistic of wet-event duration suggests timescales of 4–6 h over land and 5–7 h over the oceans. Our two different methods of estimating spatial scales suggest scales of about 90–150 km over land and 115–175 km over the oceans. It need hardly be emphasized that these numbers are simple summary measures of rich and complex structures in Figs. 2–6. Even so, they represent useful broad targets for GCMs. Simulation of Figs. 1–6 themselves, which have been generated by objective procedures, could be the next, more difficult, target.

We stress again that our principal aim is to provide *simple* local measures of the space–time characteristics of tropical deep convection. We also wish to emphasize the simple redness of much of the variability, in both space and time, that is not obvious from the figures shown thus far. This redness, and also the contrasting behavior over land and ocean, is well illustrated by the statistics in three land and three ocean areas in Fig. 7. Figure 8 shows the average spatial autocorrelation of DCA, and also the measure $D(r)$ of the statistical dependence of DCA values, as a function of spatial lag. The approximately exponential decay of these curves is consistent with that of spatial red noise. Also, a faster decay is evident over land in both panels. Each of the plotted values represents an average of $3 \times 900 = 2700$ correlation [or $D(r)$] values. To get a sense of their robustness, values were also estimated by averaging over the 225 correlation [and similarly, the $D(r)$] values in each of the 12 land and 12 ocean sub-boxes in Fig. 7.

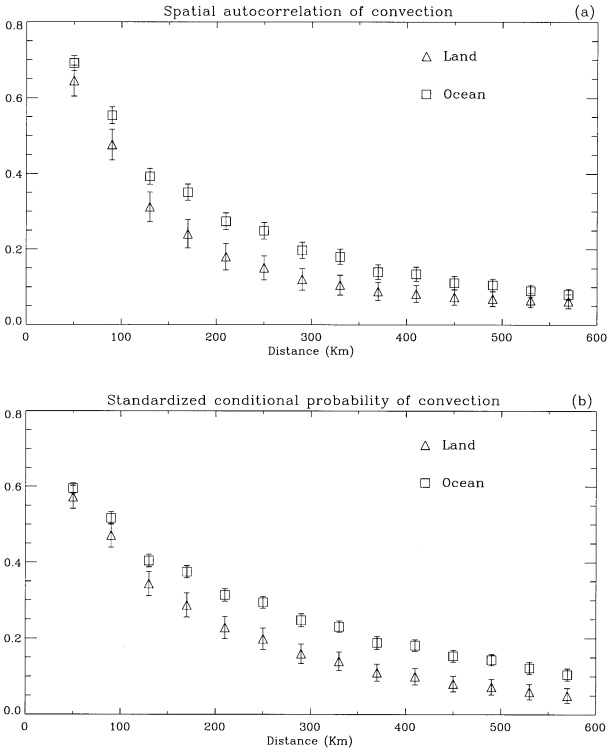

FIG. 8. Decay with distance of the (a) spatial autocorrelation of DCA over the land and ocean, and (b) statistical dependence D of DCA over the land and ocean.

The vertical ''error bars'' in Fig. 8 represent the standard deviation of these 12 estimates. The difference between the land and ocean autocorrelations, as well as between the land and ocean $D(r)$ values, is larger than these error bars.

The temporal decay of continental and oceanic convection is similarly summarized in Fig. 9, using data over the same land and ocean areas as in Fig. 7. Plotted are the histograms of wet-event durations over the land and ocean. (Note again that Fig. 2b showed the expected mean values $\langle t_w \rangle$ derived from such histograms at each grid point.) The decay with duration of these probabilities is consistent with that of temporal red noise (not shown, but see e.g., Dole and Gordon 1983). A difference between continental and oceanic values is again evident, and again greater than the error bars estimated as the standard deviation of 12 independent estimates derived from the 12 sub-boxes in Fig. 7.

Finally, some comment on the sensitivity of these results to the choice of the 240-K threshold used to define DCA in Eq. (1) is necessary. As stated at the end of section 2, some of the calculations were also repeated with thresholds of 230 and 220 K, and gave generally similar results. As the threshold was decreased to 220 K (so that only the highest clouds were considered), the timescales decreased by about an hour, but over both continents and oceans, thus leaving their relative difference unaltered. The diurnal amplitude was increased

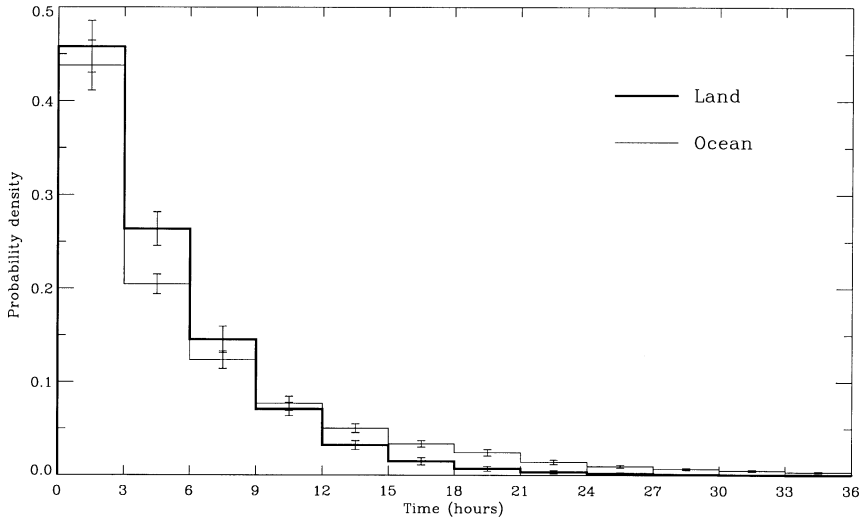

FIG. 9. Probability of duration of wet events over land and ocean.

by about 25%, but again almost uniformly, so the distinction between continents and oceans again remained more or less intact. The diurnal phase was much less sensitive.

4. Statistics of 2.8° averages

In preliminary discussions of these results at conferences and symposia, a concern was raised as to what extent they provided direct verification targets for GCMs, given the higher spatial resolution of the GCI data. To address this question, the entire analysis of the previous sections was repeated using DCA values averaged over 2.8° × 2.8° latitude–longitude grid boxes corresponding to the Gaussian grid of climate models with T42 horizontal spectral resolution. (Specifically, DCA values on the global 128 × 64 T42 Gaussian grid were obtained by averaging the 32 DCA values on the global 512 × 512 GCI grid within each T42 grid box.)

Figure 10 is in an identical format to Fig. 1, but shows the fraction of convectively active months in our 36-month dataset obtained using the spatially averaged DCA values. The pattern, in addition to resembling a smoother version of that in Fig. 1, also shows larger areas of perpetually active months. Figures 11a and 11b are likewise in an identical format to Figs. 2b and 4a, respectively, but generated using the spatially averaged DCA values. The patterns in both are similar to those in their high-resolution counterparts, but the magnitudes are generally larger. The mean durations of wet events are now approximately doubled, as are the space scales. For the diurnal cycle, however, the results do not depend strongly on resolution.

It should be emphasized that while Figs. 11a and 11b have been generated using spatially smoothed DCA values, they are not meant to be, and nor are they, merely spatially smoothed versions of Figs. 2b and 4a. If they were, the maxima in them would be attenuated rather than inflated relative to those in Figs. 2b and 4a, which is clearly not the case. Figures 11a and 11b may be

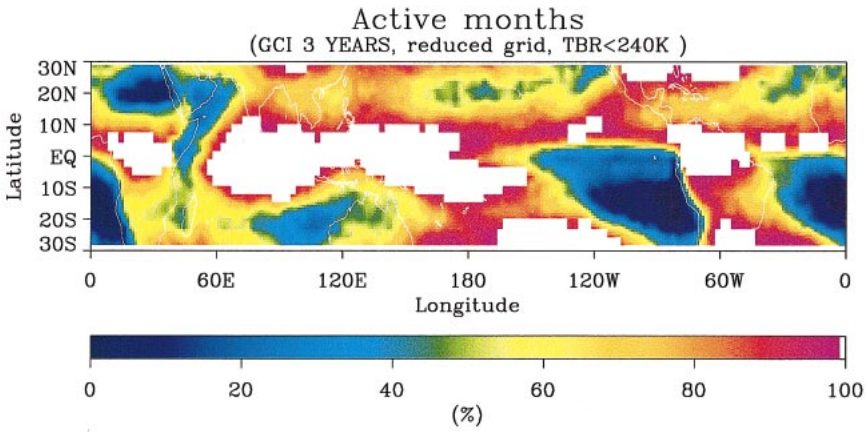

FIG. 10. As in Fig. 1, but obtained using DCA averaged over 2.8° × 2.8° boxes.

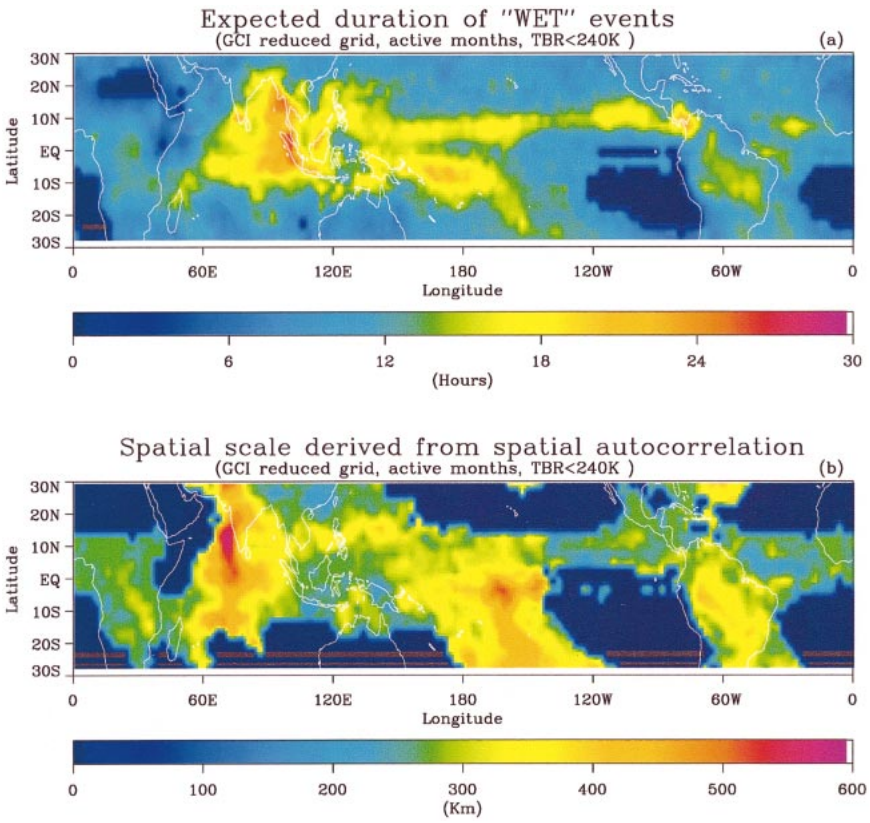

FIG. 11. (a) As in Fig. 2b but obtained using DCA averaged over 2.8° × 2.8° boxes, and (b) as in Fig. 4a but obtained using DCA averaged over 2.8° × 2.8° boxes.

more accurately viewed as resulting from the application of a low-pass space–*time* filter rather than a spatial filter alone. This is because spatially smoothing the DCA values also effectively results in *temporally* smoothing them. To understand this, consider the 32 GCI grid boxes within a T42 grid box. If it rains in only one GCI grid box in one 3-h segment and in another in the next, then there is no temporal continuity in either GCI box over 6 h; however, there is temporal continuity in the encompassing T42 box average. This temporal smoothing effect is relatively large around relatively small landmasses such as the Maritime Continent surrounded by ocean, with the result that the extensive minimum over that region in Fig. 2b is nearly ''filled in'' in Fig. 11a.

Although not as clear, the overall message from our analysis of the statistics of area-averaged DCA is nevertheless the same as in the previous sections, that both the time- and space scales of convection tend to be somewhat shorter over the continents than the oceans, and the diurnal amplitude is much larger over land, where it is comparable to the long-term mean.

The fact that the estimated time- and space scales are larger for area-averaged DCA should not be interpreted as implying that they are somehow ''arbitrary,'' and that no intrinsic time- and space scales exist. These larger estimates are entirely a result of working with artificially smoothed data. (As discussed above, the procedure is roughly equivalent to applying a low-pass filter in the wavenumber-frequency domain, which results in reduced power at both high wavenumbers and high frequencies.) It is well known, for example, that the correlation scale of temporally averaged red noise is larger than its intrinsic timescale, by an amount that increases with the length of the averaging interval. Spatial smoothing can similarly result in spuriously inflated estimates of spatial correlation scales. The time and space scales in both Figs. 11a and 11b are inflated in this sense. Even so, they represent legitimate verification targets for the statistics of 2.8° averages in GCMs. The inflationary effect is much smaller for red noise averaged over intervals comparable to or shorter than its intrinsic scale, so the scales depicted in Figs. 2b and 4a are more representative of their true values given that they are longer than the resolution of the GCI data.

5. Preliminary comparison with two GCMs

Our simple local statistical analysis was also applied to output from two atmospheric GCMs, one with high spatial and temporal resolution comparable to that of the GCI data, and the other with resolution comparable

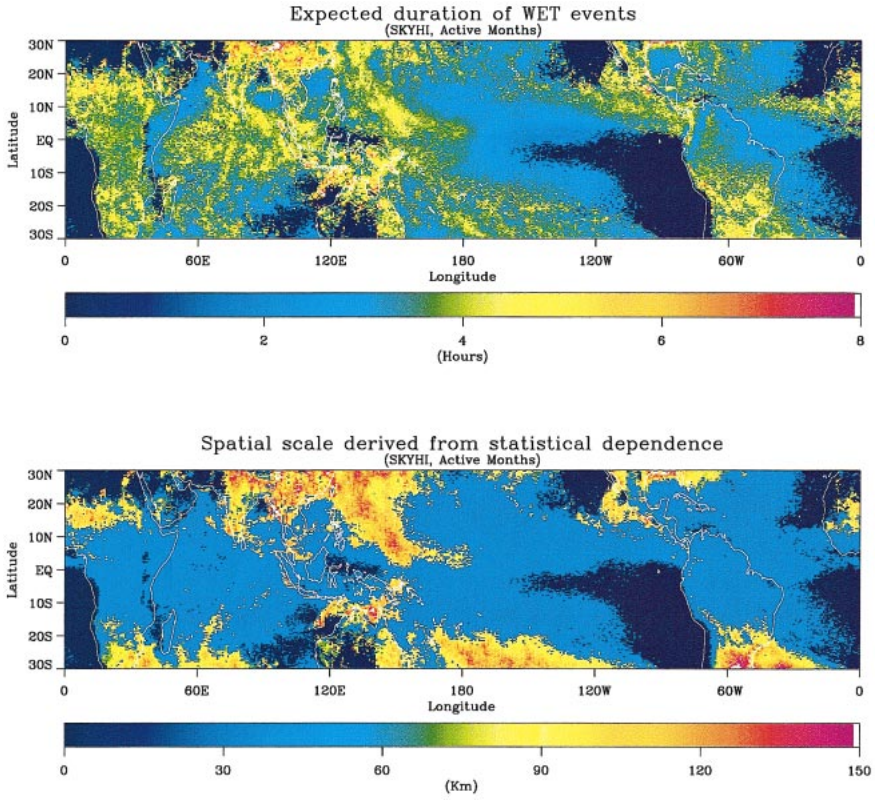

FIG. 12. (a) As in Fig. 2b but for precipitation from the high-resolution SKYHI GCM, and (b) As in Fig. 4b but for precipitation from the high-resolution SKYHI GCM.

to that of the spatially averaged GCI data discussed in the previous section.

The high-resolution GCM run we analyzed was of the N270 (0.33° lat × 0.40° lon) version of the Geophysical Fluid Dynamics Laboratory (GFDL) SKYHI model described in Hamilton et al. (1995, 1999). The model is designed primarily for stratospheric studies, and does not have a diurnal cycle. Deep convection is parameterized using a moist convective-adjustment scheme. The model output was averaged over adjacent latitudes to obtain values on a 0.33° × 0.80° grid, similar to the 0.35° × 0.70° GCI grid. Nine months of precipitation amounts over 2-h intervals, expressed in units of mm day^{-1}, were analyzed. Deep convection was distinguished from a significant background ''drizzle'' by using a threshold of 8 mm day^{-1}. A weaker threshold of 4 mm day^{-1} yielded nearly identical results (not shown).

Figures 12a and 12b are this GCM's counterparts of Figs. 2b and 4b, respectively. Over large stretches of the oceans, the timescales in Fig. 12a are 2–3 h as opposed to the 5–7 h in Fig. 2b. The discrepancy is somewhat smaller over land, but the Maritime Continent is much less obvious, perhaps because of the absence of the diurnal cycle. The disagreement of Fig. 12b with Fig. 4b is even more striking. In general, the spatial scales are much shorter in the GCM than in the GCI data (with some notable exceptions in the subtropics) and the distinctive behavior over the Maritime Continent is again missing.

Our second comparison was with a run of the CCM3.6 version of the NCAR Community Climate Model (see Kiehl et al. 1996) with a mass–flux convective parameterization described in Zhang and McFarlane (1995). The run was made at T42 resolution with a 2.8° × 2.8° Gaussian grid. Three-hourly values of model deep convective heating rates were vertically averaged from the surface to 100 mb. Figure 13 shows the time- and space scales of the model's DCH values thus obtained. The figure may be compared directly with Fig. 11, since the scales of the GCI-derived DCH are identical to those of DCA. As in the GCI data, the CCM shows relatively smaller temporal scales over the continents than the oceans, but that is where the similarity ends. Overall, the timescales are much too long in the CCM. The model is better at representing the spatial scales of deep convection, although they are much larger than in the GCI data in an equatorial zone stretching eastward from the date line to the African coast.

Finally, Fig. 14 illustrates the inability of this version of the CCM to represent realistically the temporal variability of deep convection. The top panel shows the time series of model-derived DCH during August 1983 at a grid point near 10°N, 160°E. The time series of the 2.8° × 2.8° spatially averaged GCI-derived DCH at the

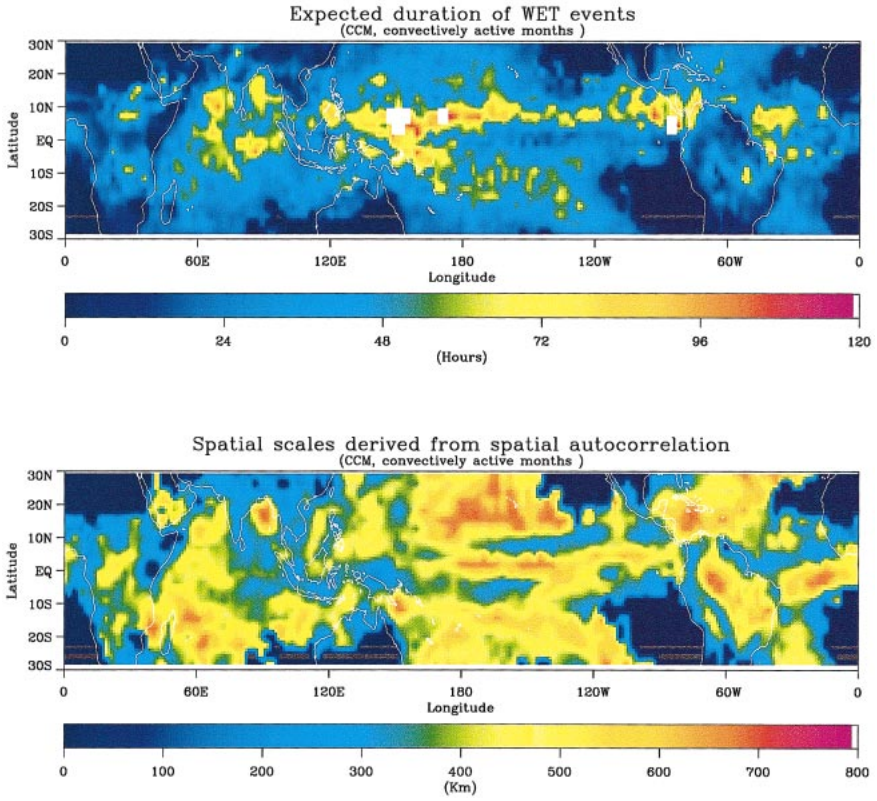

FIG. 13. As in Fig. 11 but for column-averaged deep convective heating in NCAR CCM3.6.

same point during the same month is shown in the middle panel, and the time series of the original (i.e., the spatially unaveraged) DCH is shown in the bottom panel. Given the chaotic nature of the atmosphere and the fact that the model's state on 1 August was not an observed state, the simulated and ''observed'' time series in the upper and middle panels are not strictly comparable. Nonetheless, the model's inability to capture the highly episodic character of the observed time series is clear. The deficiency would appear even more glaring if, as suggested by a reviewer, we had used a lower threshold of say 230 K to define DCA in (1). Note that the deficiency would not be obvious from inspection of monthly mean DCH values, which are comparable in the three panels.

6. Summary and concluding remarks

In this paper we focused on the *local* temporal and spatial scales of observed tropical deep convection. A multiyear cloud dataset with high spatial and temporal resolution was analyzed. In order to retain the advantages of the high resolution in space and time, no interpolation or smoothing was performed. As a consequence, very detailed features in space and time emerged in the analysis.

Our results highlight the geographical variation of the local time- and space scales of deep convection: generally shorter scales over land than ocean; and a much stronger diurnal cycle over land, strong enough to affect the long-term climate mean. Also, although the general area of the west Pacific around the Indonesian archipelago, New Guinea, and Borneo is in large part water, the convection over it behaves in several respects like over land, and justifies viewing it as an extended Maritime Continent with a distinctive shape. The distinction between continental and oceanic convection is summarized in Figs. 3, 5, 8, and 9.

In general, most of our results are not surprising, given that tropical convective cumuli have been studied extensively in field campaigns. However, most of those studies were limited in space and time. We felt the need to provide simple quantitative measures of the characteristics of deep convection in the global Tropics, and without regard to season. The availability of the multiyear GCI dataset made this possible.

Identical statistical analyses were also performed on the output from two different atmospheric GCMs: a high-resolution version of the GFDL SKYHI model and a T42 version of the NCAR CCM. Convection in the SKYHI model was found to be organized on shorter time- and space scales than in the GCI data. This is also associated with a poor organization of convection on larger scales in the GCM, especially over the west Pacific warm pool, and a poor projection on coherent large-

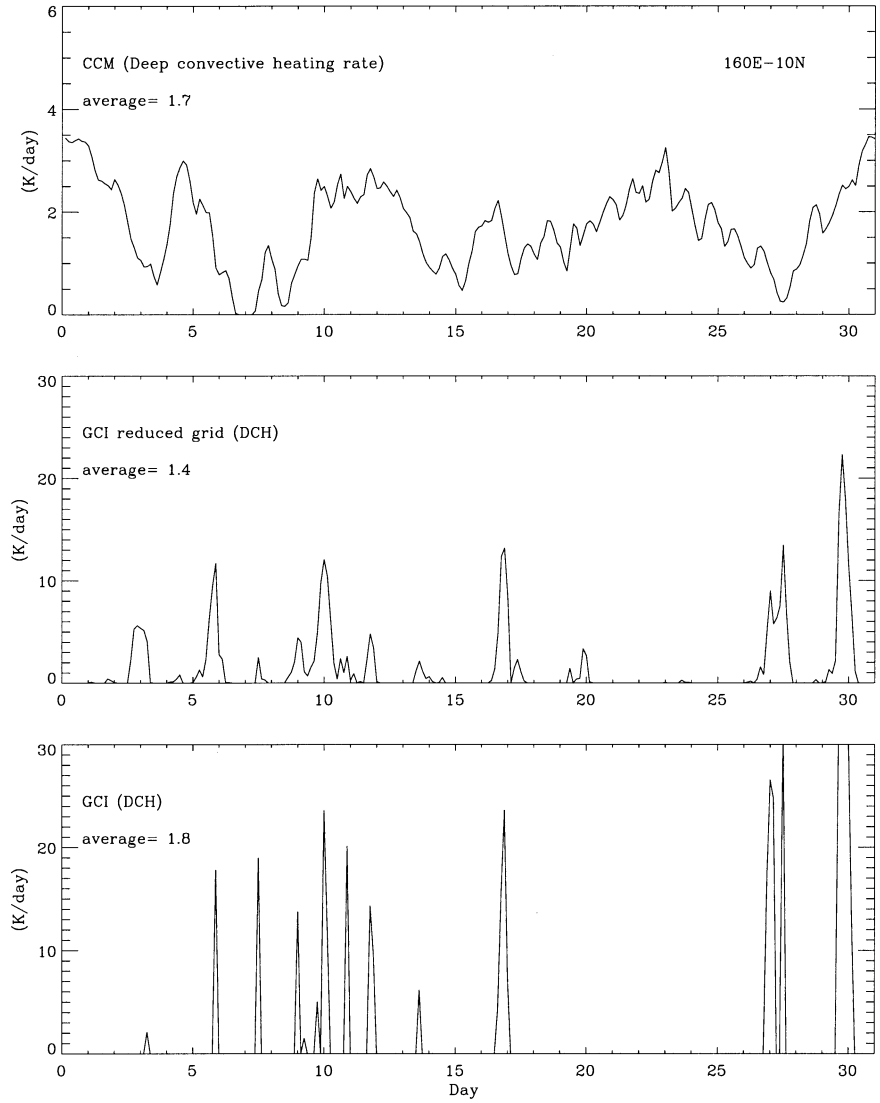

FIG. 14. Time series of deep convective heating in Aug 1983 at 10°N, 160°E from the (top) CCM3.6, (middle) the GCI data at the same coarse resolution, and (bottom) the GCI data at its full resolution.

scale equatorial wave modes. In particular, the excitation of large-scale Kelvin modes is highly underestimated, with serious implications for the simulation of the Madden–Julian oscillation (MJO). Even so, it is noteworthy that this GCM, unlike many others, simulates a lower-stratospheric zonal-wind oscillation similar to the observed quasi-biennial oscillation. A possible explanation is that the model's greater convective variability at shorter scales increases its excitation of vertically propagating gravity waves into the stratosphere. The other GCM we examined, the lower-resolution NCAR CCM, shows a systematic *overestimation* of convective spatial and temporal scales. This contributes to a significant underestimation of the overall level of tropical convective variability in the model, with implications for the simulation of the MJO and the excitation of equatorial waves on all scales (Ricciardulli and Garcia 2000; Maloney and Hartmann 2001).

Our Eulerian and isotropic spatial and temporal scales are objectively defined and are easy to compute. However, like many summary measures they are not always easy to interpret, especially in regions where the space–time variability is not well approximated as isotropic red noise. As pointed out by a reviewer, areas of off-equatorial tropical cyclone activity seem partly to underlie our finding of larger scales over the oceans, especially on the fringes of climatologically rainy areas. It may be that rain only occurs in these marginal areas when an organized depression or cyclone is present.

It should also be reiterated that our precise estimates of the time- and space scales are subject to some uncertainty, given that they are not much longer than the

space–time resolution of the GCI data. While we do not believe this limitation to be serious enough to affect any of our main conclusions, it does suggest caution when making detailed comparisons of our results with GCM output.

The analysis of this paper provides a compact description of deep convection in the Tropics. Some of its characteristics presented here are obscured in the long-term averages that are often employed to validate models. Nonetheless, they appear important enough that they should probably be captured in GCMs. Our statistical analysis can be easily applied to GCM output. It provides a simple *regional* description of tropical convective variability that could be useful in GCM evaluation and perhaps even in guiding GCM improvement.

Acknowledgments. The authors are grateful to Murry Salby for providing the GCI data, and to Kevin Hamilton for providing the SKYHI model output. Discussions with Jim Hack and Rolando Garcia of NCAR and John Bergman and Harry Hendon of CDC were especially helpful. The constructive criticism of all three referees resulted in substantial improvement of the manuscript.

REFERENCES

Arakawa, A., 1993: Closure assumption in the cumulus parameterization problem. *The Representation of Cumulus Convection in Numerical Models, Meteor. Monogr.,* No. 46, Amer. Meteor. Soc., 1–15.

——, and W. H. Schubert, 1974: Interaction of cumulus cloud ensemble with the large-scale environment, Part I. *J. Atmos. Sci.*, **31,** 674–701.

Bergman, J. W., and M. L. Salby, 1994: Equatorial wave activity derived from fluctuations in observed convection. *J. Atmos. Sci.*, **51,** 3791–3806.

——, and ——, 1996: Diurnal variations of cloud cover and their relationship to climatological conditions. *J. Climate,* **9,** 2802–2820.

Betts, A. K., and M. J. Miller, 1986: A new convective adjustment scheme. Part I: Observational and theoretical basis. *Quart. J. Roy. Meteor. Soc.,* **112,** 677–691.

Boer, E. R., and V. Ramanathan, 1997: Lagrangian approach for deriving cloud characteristics from satellite observations and its implications to cloud parameterization. *J. Geophys. Res.,* **102,** 21 383–21 399.

Chen, S. S., and R. A. Houze, 1997: Diurnal variation and life-cycle of deep convective systems over the tropical Pacific warm pool. *Quart. J. Roy. Meteor. Soc.*, **123,** 357–388.

Desbois, M., T. Kayiranga, B. Gnamien, S. Guessous, and L. Picon, 1988: Characterization of some elements of the Sahelian climate and their interannual variations for July 1983, 1984 and 1985 from the analysis of Meteosat ISCCP data. *J. Climate,* **1,** 867–904.

Dole, R. M., and N. D. Gordon, 1983: Persistent anomalies of the extratropical Northern Hemisphere wintertime circulation—Geographical distribution and regional persistence characteristics. *Mon. Wea. Rev.,* **111,** 1567–1586.

Duvel, J. P., 1989: Convection over tropical Africa and the Atlantic Ocean during northern summer. Part I: Interannual and diurnal variations. *Mon. Wea. Rev.,* **117,** 2782–2799.

——, and R. S. Kandel, 1988: Tropospheric response to tropical diurnal forcing observed by METEOSAT. *Geophys. Res. Lett.*, **15,** 788–791.

Fu, R., A. D. Del Genio, and W. B. Rossow, 1990: Behavior of deep convective clouds in the tropical Pacific deduced from ISCCP radiances. *J. Climate,* **3,** 1129–1152.

Gates, W. L., and Coauthors, 1999: An overview of the results of the Atmospheric Model Intercomparison Project (AMIP I). *Bull. Amer. Meteor. Soc.,* **80,** 29–56.

Hamilton, K., R. J. Wilson, J. D. Mahlman, and L. J. Umscheid, 1995: Climatology of the SKYHI troposphere–stratosphere–mesosphere general circulation model. *J. Atmos. Sci.*, **52,** 5–43.

——, ——, and R. Hemler, 1999: Middle atmosphere simulated with high vertical and horizontal resolution versions of a GCM: Improvement in the cold pole bias and generation of a QBO-like oscillation in the Tropics. *J. Atmos. Sci.,* **56,** 3829–3846.

Hendon, H. H., and K. Woodberry, 1993: The diurnal cycle of tropical convection. *J. Geophys. Res.,* **98,** 16 623–16 637.

Hess, P. G., D. Battisti, and P. Rasch, 1993: Maintenance of the intertropical convergence zones and the large-scale tropical circulation on a water-covered earth. *J. Atmos. Sci.,* **50,** 691–713.

Horel, J. D., and J. M. Wallace, 1981: Planetary-scale atmospheric phenomenon associated with the Southern Oscillation. *Mon. Wea. Rev.,* **109,** 2080–2092.

Hoskins, B. J., and D. J. Karoly, 1981: The steady linear response of a spherical atmosphere to thermal and orographic forcing. *J. Atmos. Sci.,* **38,** 1179–1196.

Imaoka, K., and R. W. Spencer, 2000: Diurnal variation of precipitation observed by TRMM/TMI combined with SSM/I. *J. Climate,* **13,** 4149–4158.

James, I. N., and D. L. T. Anderson, 1984: The seasonal mean flow and distribution of large-scale weather systems in the southern hemisphere—The effect of moisture transports. *Quart. J. Roy. Meteor. Soc.,* **110,** 943–966.

Joyce, R., and P. A. Arkin, 1997: Improved estimates of tropical and subtropical precipitation using GOES precipitation index. *J. Atmos. Oceanic Technol.,* **14,** 997–1011.

Kiehl, J. T., J. J. Hack, G. B. Bonan, B. A. Boville, B. P. Briegleb, D. L. Williamson, and P. J. Rasch, 1996: Description of NCAR Community Climate Model (CCM3). Tech. Note NCAR/TN-420+STR, Boulder, CO, 152 pp.

Kuo, H. L., 1974: Further studies of the properties of cumulus convection on the large scale flow. *J. Atmos. Sci.,* **31,** 1232–1240.

Laing, A. G., and J. M. Fritsch, 1997: The global population of mesoscale convective complexes. *Quart. J. Roy. Meteor. Soc.,* **123,** 389–405.

Maloney, E. D., and D. L. Hartmann, 2001: The sensitivity of intraseasonal variability in the NCAR CCM3 to changes in convective parameterization. *J. Climate,* **14,** 2015–2034.

Manabe, S., J. Smagorinsky, and R. F. Strickler, 1965: Simulated climatology of a general circulation model with a hydrologic cycle. *Mon. Wea. Rev.,* **93,** 769–798.

Opsteegh, J. D., and H. M. Van den Dool, 1980: Seasonal differences in the stationary response of a linearized primitive equation model: Prospects for long-range weather forecasting? *J. Atmos. Sci.,* **37,** 2169–2185.

Palmer, T. N., and D. L. T. Anderson, 1994: The prospects for seasonal forecasting—A review paper. *Quart. J. Roy. Meteor. Soc.,* **120,** 755–793.

Peng, P., A. Kumar, A. G. Barnston, and L. Goddard, 2000: Simulation skills of the SST-forced global climate variability of the NCEP-MRF9 and the Scripps/MPI ECHAM3 models. *J. Climate,* **13,** 3657–3679.

Ray, E. A., J. R. Holton, E. F. Fishbein, L. Froidevaux, and J. Waters, 1994: The tropical semiannual oscillation in temperature and ozone as observed by MLS. *J. Atmos. Sci.,* **51,** 3045–3052.

Ricciardulli, L., and R. R. Garcia, 2000: The excitation of equatorial waves by deep convection in the NCAR Community Climate Model (CCM3). *J. Atmos. Sci.,* **57,** 3461–3487.

Richards, F., and P. A. Arkin, 1981: On the relationship between satellite-observed cloud cover and precipitation. *Mon. Wea. Rev.,* **109,** 1081–1093.

Salby, M. L., H. H. Hendon, K. Woodberry, and K. Tanaka, 1991:

Analysis of global cloud imagery from multiple satellites. *Bull. Amer. Meteor. Soc.,* **72,** 467–480.

Sardeshmukh, P. D., and B. J. Hoskins, 1988: The generation of global rotational flow by steady idealized tropical divergence. *J. Atmos. Sci.,* **45,** 1228–1251.

——, G. P. Compo, and C. Penland, 2000: Changes of probability associated with El Niño. *J. Climate,* **13,** 4268–4286.

Schiffer, R. A., and W. B. Rossow, 1983: The International Satellite Cloud Climatology Project (ISCCP): The first project of the World Climate Research Program. *Bull. Amer. Meteor. Soc.,* **64,** 779–784.

Slingo, J., and Coauthors, 1994: Mean climate and transience in the tropics of the UGAMP GCM: Sensitivity to convective parameterization. *Quart. J. Roy. Meteor. Soc.,* **120,** 881–922.

——, and Coauthors, 1996: Intraseasonal oscillations in 15 atmospheric general circulation models: Results from an AMIP diagnostic subproject. *Climate Dyn.,* **12,** 325–357.

Tanaka, K. H., K. Woodberry, H. H. Hendon, and M. L. Salby, 1991: Assimilation of global cloud imagery from multiple satellites. *J. Atmos. Oceanic Technol.,* **8,** 613–626.

Tiedtke, M., 1989: A comprehensive mass flux scheme for cumulus parameterization in large-scale models. *Mon. Wea. Rev.,* **117,** 1779–1800.

Ting, M., and P. D. Sardeshmukh, 1993: Factors determining the extratropical response to equatorial diabatic heating anomalies. *J. Atmos. Sci.,* **50,** 907–918.

Tung, K. K., and H. Yang, 1994: Global QBO in circulation and ozone. Part I. Reexamination of observational evidence. *J. Atmos. Sci.,* **51,** 2699–2707.

Wheeler, M., and G. N. Kiladis, 1999: Convectively coupled equatorial waves: Analysis of clouds and temperature in the wavenumber–frequency domain. *J. Atmos. Sci.,* **56,** 374–399.

Winkler, C. R., M. Newman, and P. D. Sardeshmukh, 2001: A linear model of wintertime low-frequency variability. Part I: Formulation and forecast skill. *J. Climate,* **14,** 4474–4494.

Woodberry, K., K. Tanaka, H. H. Hendon, M. L. Salby, 1991: An interactive system for analysis of global cloud imagery. *J. Atmos. Oceanic Technol.,* **8,** 627–638.

Yang, G. Y., and J. Slingo, 2001: The diurnal cycle in the Tropics. *Mon. Wea. Rev.,* **129,** 784–801.

Zhang, G. J., and N. A. McFarlane, 1995: Sensitivity of climate simulations to the parameterization of cumulus convection in the Canadian Centre General Circulation Model. *Atmos.–Ocean,* **33,** 407–446.